

# Proactive Pseudo-Intervention: Causally Informed Contrastive Learning For Interpretable Vision Models

Dong Wang, Yuewei Yang, Chenyang Tao, Fanjie Kong, Ricardo Henao, Lawrence Carin

dong.wang363, yuewei.yang, chenyang.tao, fanjie.kong, ricardo.henao, lcarin@duke.edu

## Abstract

*Deep neural networks have shown significant promise in comprehending complex visual signals, delivering performance on par or even superior to that of human experts. However, these models often lack a mechanism for interpreting their predictions, and in some cases, particularly when the sample size is small, existing deep learning solutions tend to capture spurious correlations that compromise model generalizability on unseen inputs. In this work, we propose a contrastive causal representation learning strategy that leverages proactive interventions to identify causally-relevant image features, called Proactive Pseudo-Intervention (PPI). This approach is complemented with a causal salience map visualization module, i.e., Weight Back Propagation (WBP), that identifies important pixels in the raw input image, which greatly facilitates the interpretability of predictions. To validate its utility, our model is benchmarked extensively on both standard natural images and challenging medical image datasets. We show this new contrastive causal representation learning model consistently improves model performance relative to competing solutions, particularly for out-of-domain predictions or when dealing with data integration from heterogeneous sources. Further, our causal saliency maps are more succinct and meaningful relative to their non-causal counterparts.*

## 1. Introduction

Deep neural networks hold great promise in applications requiring the analysis and comprehension of complex imagery. Recent advances in hardware, network architectures, and model optimization, along with the increasing availability of large-scale annotated datasets [32, 12, 11], have enabled these models to match and sometimes outperform human experts on a number of tasks, including natural image classification [33], objection recognition [21], disease diagnosis [46], and autonomous driving [8], among others.

Deep learning solutions have been positively recognized for their ability to learn *black-box* models in a purely data driven manner. However, their very nature makes them less

credible for their inability to communicate their reasoning for making predictions in a way that is comprehensible to humans. This suggests that in order to stimulate widespread use of deep learning models, a means of interpreting predictions is necessary, particularly in applications where predictions are consequential, *e.g.*, in healthcare. Moreover, naive interpretation of model predictions is especially concerning because deep learning models tend to assimilate spurious correlations that do not necessarily capture the causal relationship between the input (image) and output (label) of the model. This issue is particularly notable in small-sample-size (low supervision) scenarios or when the sources of non-informative variation are overwhelming, thus likely to cause severe overfitting. As a result, lack of interpretability or a poor implementation of a model with interpretable predictions can often lead to catastrophic failures on deployment [19, 61].

A growing recognition of the issues associated with the lack of interpretable predictions is well documented [1, 27, 44]. Such phenomenon has energized researchers to actively seek creative solutions. Among these, two streams of work, namely *saliency mapping* (SM) [65, 52, 10] and *causal representation learning* (CRL) [29, 62, 2], stand out as some of the most promising directions. Specifically, SM encompasses techniques for *post hoc* visualizations on the input (image) space to facilitate interpretation of model predictions. This is done by projecting the key features used in prediction back to the input space, resulting in the commonly known *saliency maps*. These techniques typically rely on the notion of sensitivity of the input to changes in the model output, to derive a map of image regions that are important for prediction. Importantly, these maps do not directly contribute to model learning. Alternatively, CRL solutions are built on the principles of establishing invariances from the data, which require the identification of sources of variation that are spuriously associated with the model output (labels). CRL models, while emphasizing the differences between causation and correlation, are not subject to the rigor of causal inference approaches, because their goal is not to obtain accurate causal effect estimates but rather to produce robust models with better generalization ability

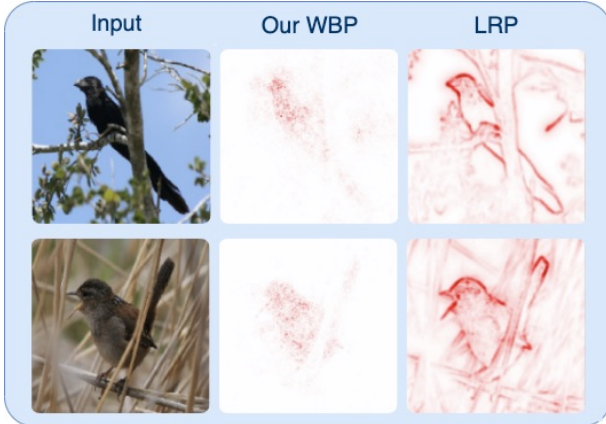


Figure 1: Saliency maps generated by the state-of-the-art *layer-wise relevance propagation* (LRP) and the proposed *Weight Back Propagation* (WBP). LRP emphasizes the background (habitat, *e.g.*, tree, ground) that are spuriously correlated with the bird species, while the causally informed WBP mostly focuses on the bird anatomy.

relative to their naively learned counterparts [2].

In this work, we present a solution that accounts for the needs of causal representation identification and visual verification. Our key insight is the derivation of causally-informed saliency maps, which facilitate visual verification of model predictions *and* enable learning that is robust to nuisance (non-causal) invariances. While true causation can only be established through experimental interventions, we leverage tools from contrastive representation learning to generate pseudo-interventions from observational data, which are motivated by the following causal argument: the target label will be changed only if causally-relevant features are perturbed.

In Figure 1 we present an example of saliency maps to illustrate the benefits of producing causally-informed saliency maps. In this scenario, the task is to classify two bird species (A and B) from natural images. Due to the differences in their natural habitats, A-birds are mostly seen resting on trees, while B-birds are more commonly found among bulrushes. A deep model, trained naively, will tend to associate the background characteristics with the labels, knowing these strongly correlate with the bird species (labels) in the training set. As a result, state-of-the-art layer-wise relevance propagation (LRP) saliency maps [4] from this model tend to emphasize background features as opposed to (more subtle) differences in bird anatomy. Further, if we were provided with an image of a bird in an environment foreign to the images in the training set, the model will be unable to make a reliable prediction (or if *different* types of animals were in the same environments, they could be confused with bird A or B). This generalization issue, which worsens with small sample sizes, is evidence of the lack of

robustness of the model. Alternatively, a causally-informed module of our PPI, like the proposed Weight Back Propagation (WBP), will successfully focus on the bird anatomy, and thus will be robust to environmental changes captured in the input images.

This paper presents an easy-to-implement strategy called *Proactive Pseudo-Intervention* (PPI) that addresses causally-informed reasoning, robust learning, and interpretation of model predictions in a unified framework. Importantly, PPI seamlessly combines saliency mapping and contrastive interventions to guide model learning. The contributions of this paper are summarized as follows:

- An end-to-end contrastive causal representation learning strategy that employs proactive interventions to identify causally relevant features.
- A fast and architecture-agnostic saliency mapping module called *Weight Back Propagation* (WBP), that delivers accurate and faithful interpretation of predictions.
- Experiments demonstrating significant performance gains of PPI relative to competing solutions, especially on model visualization, out-of-domain predictions, and data integration with heterogeneous sources.

## 2. Background

**Visual Explanations** Saliency mapping collectively refers to a family of techniques to understand and interpret black-box image classification models, such as deep neural networks [1, 27, 44]. These methods project the model understanding of the targets, *i.e.*, labels, and their predictions back to the input space, which allows for the visual inspection of automated reasoning and for the communication of predictive visual cues to the user or human expert, thus establishing a visual relationship between images and predictions aimed to build trust in deep-learning-based systems.

In this study, we focus on *post hoc* saliency mapping strategies, where saliency maps are constructed given an arbitrary (trained) prediction model, as opposed to relying on customized model architectures for interpretable predictions [19, 61], or to train a separate module to explicitly produce model explanations [19, 22, 6, 18, 51]. Popular solutions under this category include activation mapping [66, 49], relevance propagation [4] and input sensitivity analysis [51]. As we will show in our experiments, these approaches fail to yield causal explanations of the outcome, and are therefore unable to satisfactorily address the challenges discussed above.

Our work is in a similar spirit to [18, 10, 6, 58], where meaningful perturbations have been applied to the image during model training, to improve prediction and facilitate interpretation. Such perturbations are usually computed by solving an optimization for each image, and consequently

they are costly in practice and also do not address the challenges from spurious features. Very recently, exploratory effort has been made to leverage the tools from counterfactual reasoning [22] and causal analysis [41] to derive visual explanations, but do not lend insights back to model training. Our work represents a fast, principled solution that overcomes the above limitations.

**Contrastive Learning.** There has been growing interest in exploiting contrastive learning (CL) techniques for representations learning [40, 9, 25, 30, 57]. Originally devised for density estimation [24], CL exploits the idea of *learning by comparison* to capture the subtle features of data, *i.e.*, positive examples, by contrasting them with negative examples drawn from a carefully crafted noise distribution. From the perspective of representation learning, these techniques aim to avoid representation collapse, or to promote representation consistency, for downstream tasks. Recent developments, both empirical and theoretical, have connected CL to information-theoretic foundations [57, 23], thus establishing them as a suite of *de facto* solutions for unsupervised representation learning [9, 25].

The basic form of CL is essentially a binary classification task specified to discriminate positive and negative examples. In such a scenario, the binary classifier is known as the critic function. Maximizing the discriminative power wrt the critic and the representation sharpens the feature encoder. Critical to the success of CL is the choice of appropriate noise distribution, where the challenging negatives, *i.e.*, those negatives that are more similar to positive examples, are often considered more effective contrasts in terms of learning efficiency, as the model will work harder to mine and refine the representation. In its more generalized form, CL can naturally repurpose the predictor and loss functions without introducing a new critic [57]. Notably, current CL methods are not immune to spurious associations, a point we wish to improve in this work.

**Causality and Interventions.** While many powerful computer vision models excel at comprehending complex scenes for predictive purposes, their success often entails the over-exploitation of visual cues. Perturbations to external factors, *e.g.*, background, lighting, viewing angles, may drastically alter their predictions, while human recognition is less susceptible to such variations. This happens because standard machine learning models base their decision on correlations, as opposed to performing causal reasoning. From a causality perspective, observational data are in general affected by (unknown) confounding factors, and consequently are unable to inform the structural dependencies for causal decisions. Formally, such difference is best explained with the *do*-notation [42]:  $\mathbb{P}(Y|do(x)) = \sum_z \mathbb{P}(Y|X = x, z)\mathbb{P}(z)$ , where we identify  $x$  as the features, *e.g.*, an object in the image, and  $z$  as the con-

founders, *e.g.*, background in the example above. In the causality literature,  $z$  is commonly referred to as the treatment [2, 20]. We note that  $\mathbb{P}(Y|do(x))$  is fundamentally different from the association reasoning rule  $\mathbb{P}(Y|X = x) = \sum_z \mathbb{P}(Y|X = x, z)\mathbb{P}(z|X = x)$ .

To acquire causal knowledge, the learning procedure requires experimental *interventions* to intentionally block the causal links between the features  $x$  and confounders  $z$ . This action is typically implemented by explicitly intervening the experiments by fixing  $x$ , and then observing how it affects the outcome  $y$ . Unfortunately, carrying out real interventional studies, *i.e.*, randomized control trials, is oftentimes not a feasible option for practical considerations, *e.g.*, cost and ethics. Fortunately, in the computer vision scenario, we can apply synthetic interventions to the observational data to uncover the underlying causal features. Specifically, we proactively edit  $x$  and its corresponding label  $y$  in a data-driven fashion to encourage the model to only respond to causal associations.

In recent years, the significance of establishing causality in machine learning models has received growing appreciation [47]. Via promoting invariance [2], such causally inspired solutions boast superior robustness to superficial features that do not generalize [60]. In particular, [55, 64] demonstrated the importance and effectiveness of accounting for interventional perspectives. Our work brings these causal views to construct a simple solution that explicitly optimizes visual interpretation and model robustness.

### 3. Proactive Pseudo-Intervention

Below we describe the construction of *proactive pseudo-intervention* (PPI), a causally-informed contrastive learning scheme that seeks to simultaneously improve the accuracy, robustness, generalization and interpretability of deep-learning-based computer vision models.

The PPI model, schematically summarized in Figure 2, consists of three main components: (i) a saliency mapping module that highlights causally relevant features; (ii) an intervention module that synthesizes contrastive samples; and (iii) the prediction module, which is standard in recent vision models, *e.g.*, VGG [53], ResNet [26], and Inception Net [56]. Motivated by the discussion from the introduction, PPI establishes a feedback loop between the saliency map module and the prediction module, which is interfaced by the synthesized contrastive examples from the intervention module. Under this configuration, the prediction module is encouraged to modify its predictions only when provided with causally-relevant synthetic interventions. Note that components (i) and (ii) do not involve any additional parameters or neural network modules, which makes our strategy readily applicable to the training of virtually any vision task without major customization. Details of these building blocks are given below.

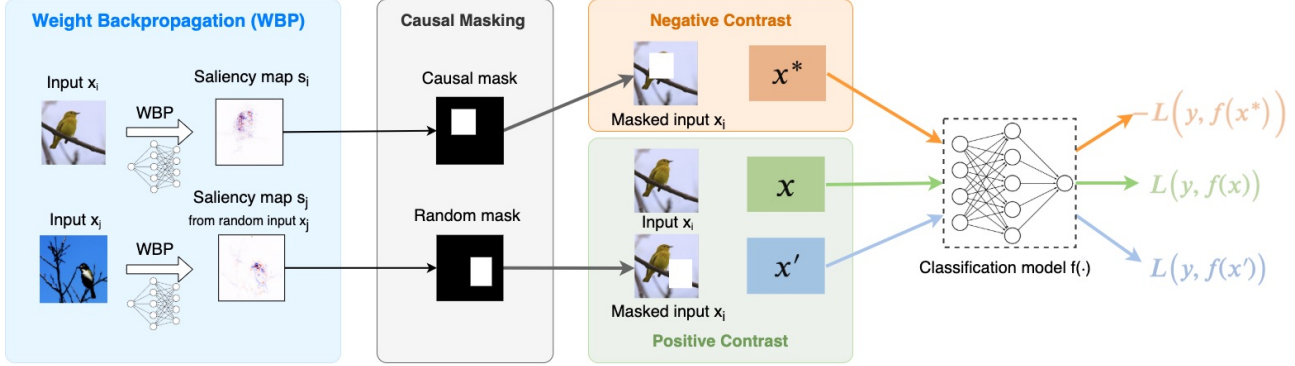


Figure 2: Illustration of the Proactive Pseudo-Intervention (PPI) learning strategy. Saliency maps are obtained via WBP (Left), contrastive interventions are created from masked inputs (Middle), and predictions are obtained from a classification model (Right).

### 3.1. Synthetic causal contrastive interventions

Key to our formulation is the design of a synthetic intervention strategy that generates contrastive examples to reinforce causal relevance. Given a causal saliency map  $s_m(\mathbf{x})$  for an input  $\mathbf{x}$  wrt label  $y = m$ , where  $m = 1, \dots, M$ , and  $M$  is the number of classes, the synthetic intervention consists of removing (replacing with zero) the causal information from  $\mathbf{x}$  contained in  $s_m(\mathbf{x})$ , and then using it as the contrastive learning signal.

For now, let us assume the causal salience map  $s_m(\mathbf{x})$  is known; the procedure to obtain the saliency map will be addressed in the next section. For notational clarity, we use subscript  $i$  to denote entities associated with the  $i$ -th training sample, and omit the dependency on learnable parameters. To remove causal information from  $\mathbf{x}_i$  and obtain a negative contrast  $\mathbf{x}_i^*$ , we apply the following *soft-masking* transformation

$$\mathbf{x}_i^* = \mathbf{x}_i - T(s_m(\mathbf{x}_i)) \odot \mathbf{x}_i, \quad (1)$$

where  $T(\cdot)$  is a differentiable masking function and  $\odot$  denotes element-wise (Hadamard) multiplication. Specifically, we use the thresholded sigmoid as the masking function:

$$T(s_m(\mathbf{x}_i)) = \frac{1}{1 + \exp(-\omega(s_m(\mathbf{x}_i) - \sigma))}, \quad (2)$$

where  $\sigma$  and  $\omega > 0$  are the threshold and scaling parameters, respectively. We set the scaling  $\omega$  so that  $T(s)$  will result in a sharp transition from 0 to 1 near  $\sigma$ . Using (1) we define the contrastive loss as

$$L_{con}(\theta) = \sum_i \ell(\mathbf{x}_i^*, \neg y; f_\theta), \quad (3)$$

where  $f_\theta$  is the prediction model,  $\ell(\mathbf{x}, y; f_\theta)$  is the loss function we wish to optimize, *e.g.* cross entropy, and  $\neg$  is used to denote that the original class label has been flipped.

In the binary case,  $\neg y = 1 - y$ , and in the multi-class case it can be interpreted accordingly, *e.g.*, using a one *vs.* others cross entropy loss. In practice, we set  $\ell(\mathbf{x}, y; f_\theta) = -\ell(\mathbf{x}, y; f_\theta)$ . We will show in the experiments that this simple and intuitive causal masking strategy works well in practice (see Tables 3 and 5, and Figure 5). Alternatively, we also consider a *hard-masking* approach in which a minimal bounding box covering the thresholded saliency map is removed. See the Appendix for details.

Note that we are making the implicit assumption that the saliency map is uniquely determined by the prediction model  $f_\theta$ . While optimizing (3) explicitly attempts to improve the fit of the prediction model  $f_\theta$ , it also implicitly informs the causal saliency mapping. This is sensible because if a prediction is made using non-causal features, which implies the associated saliency map  $s_m(\mathbf{x})$  is also non-causal, then we should expect that after applying  $s_m(\mathbf{x})$  to  $\mathbf{x}$  using (1), we can still expect to make the correct prediction, *i.e.*, the true label, for both positive (the original) and negative (the intervened) samples.

**Saliency map regularization.** Note that naively optimizing (3) can lead to degenerate solutions for which any saliency map that satisfies the causal sufficiency, *i.e.*, encompassing all causal features, is a valid causal saliency map. For example, a trivial solution where the saliency map covers the entire image may be considered causal. To protect against such degeneracy, we propose to regularize the  $L_1$ -norm of the saliency map to encourage succinct (sparse) representations, *i.e.*,  $L_{reg} = \|s_m\|_1$ , for  $m = 1, \dots, M$ .

**Adversarial contrasts.** Another concern with solely optimizing (3) is that models can easily overfit to the intervention, *i.e.*, instead of learning to capture causal relevance, the model learns to predict interventional operations. For example, the model can learn to change its prediction when it detects that the input has been intervened, regardless of whether the image is missing causal features. So motivated,

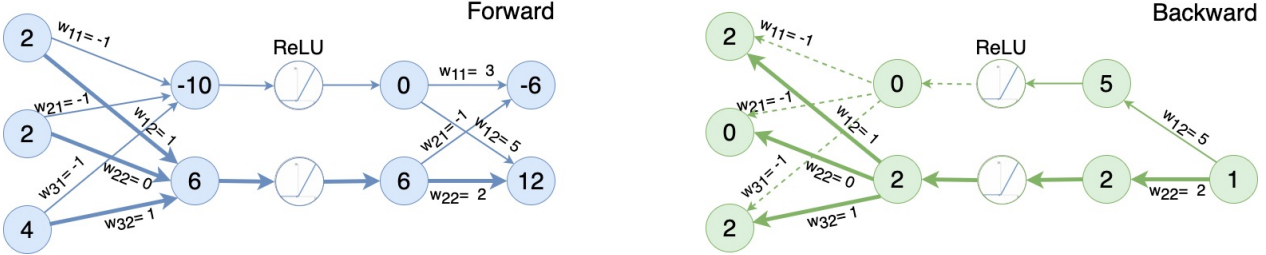


Figure 3: Illustration of the Weight Backpropagation (WBP) through a fully connected layer with ReLU activation layer.

Table 1: WBP update rules for common transformations.

Transformation	$G(\cdot)$
Activation Layer	$\tilde{W}^l = h \circ \tilde{W}^{l+1}$
FC Layer	$\tilde{W}^l = \tilde{W}^{l+1}W^l$
Convolutional Layer	$\tilde{W}^l = \tilde{W}^{l+1} \otimes [W^l]_{flip_{2,3}}^{T_{0,1}}$
BN Layer	$\tilde{W}^l = \frac{\tilde{W}^{l+1}}{\sigma} \gamma$
Pooling Layer	Relocate/Distribute $\tilde{W}^{l+1}$

we introduce adversarial contrasts:

$$\mathbf{x}'_i = \mathbf{x}_i - T(\mathbf{s}_m(\mathbf{x}_j)) \odot \mathbf{x}_i, \quad i \neq j, \quad (4)$$

where we intervene with a *false* saliency map, *i.e.*,  $\mathbf{s}_m(\mathbf{x}_j)$  is the saliency map from a different input  $\mathbf{x}_j$ , while still encouraging the model to make the correct prediction via

$$L_{ad}(\theta) = \sum_i \ell(\mathbf{x}'_i, y; f_\theta), \quad (5)$$

where  $\mathbf{x}'_i$  is the adversarial contrast. The complete loss for the proposed model,  $L = L_{cls} + L_{con} + L_{reg} + L_{ad}$ , consists of the contrastive loss in (3), the regularization loss,  $L_{reg}$ , and the adversarial loss in (5).

### 3.2. Saliency Weight Backpropagation

In order to generate saliency maps that inform causal features in the (raw) pixel space, we propose to evaluate the individual contributions from each pixel to the final class-specific prediction. To this end, below we describe Weight Back Propagation (WBP), a computationally efficient scheme for saliency mapping applicable to arbitrary neural architectures.

To simplify our presentation, we first consider a vector input and a linear mapping. Let  $\mathbf{x}^l$  be the internal representation of the data at the  $l$ -th layer, with  $l = 0$  being the input layer, *i.e.*,  $\mathbf{x}^0 = \mathbf{x}$ , and  $l = L$  being the penultimate *logit* layer prior to the softmax transformation, *i.e.*,  $\mathbb{P}(y|\mathbf{x}) = \text{softmax}(\mathbf{x}^L)$ . To assign the relative importance to each hidden unit in the  $l$ -th layer, we notationally collapse all transformations after  $l$  into an operator denoted by

$\tilde{W}^l$ , which we call the *saliency matrix*, satisfying,

$$\mathbf{x}^L = \tilde{W}^l \mathbf{x}^l, \quad \forall l \in [0, \dots, L], \quad (6)$$

where  $\mathbf{x}^L$  is an  $M$ -dimensional vector corresponding to the  $M$  distinct classes in  $y$ . Though presented in a matrix form in a slight abuse of notation, *i.e.*, the instantiation of the operator  $\tilde{W}^l$  effectively depends on the input  $\mathbf{x}$ , thus all nonlinearities have been effectively absorbed into it. We posit that for an object associated with a given label  $y = m$ , its causal features are subsumed in the interactions between the  $m$ -th row of  $\tilde{W}^0$  and input  $\mathbf{x}$ , *i.e.*,

$$[\mathbf{s}_m(\mathbf{x})]_k = [\tilde{W}^0]_{mk} [\mathbf{x}]_k, \quad (7)$$

where  $[\mathbf{s}_m(\mathbf{x})]_k$  denotes the  $k$ -th element of the saliency map  $\mathbf{s}_m(\mathbf{x})$  and  $[\tilde{W}^0]_{mk}$  is a single element of  $\tilde{W}^0$ . A key observation for computation of  $\tilde{W}^l$  is that it can be done recursively. Specifically, let  $g_l(\mathbf{x}^l)$  be the transformation at the  $l$ -th layer, *e.g.*, an affine transformation, convolution, activation, normalization, *etc.*, then it holds that

$$\tilde{W}^{l+1} \mathbf{x}^{l+1} = \tilde{W}^{l+1} g_l(\mathbf{x}^l) = \tilde{W}^l \mathbf{x}^l. \quad (8)$$

This allows for recursive computation of  $\tilde{W}^l$  via

$$\tilde{W}^l = G(\tilde{W}^{l+1}, g_l), \quad \tilde{W}^L = 1, \quad (9)$$

where  $G(\cdot)$  is the update rule. We list the update rules for common transformations in deep networks in Table 1, with corresponding derivations detailed below.

**Fully-connected (FC) layer.** The FC transformation is the most basic operation in deep neural networks. Below we omit the bias term as it does not directly interact with the input. Assuming  $g_l(\mathbf{x}^l) = W^l \mathbf{x}^l$ , it is readily seen that

$$\tilde{W}^{l+1} \mathbf{x}^{l+1} = \tilde{W}^{l+1} g_l(\mathbf{x}^l) = (\tilde{W}^{l+1} W^l) \mathbf{x}^l, \quad (10)$$

so  $\tilde{W}^l = \tilde{W}^{l+1} W^l$ . See Figure 3 for a graphical illustration with standard affine mapping and ReLU activation.

**Nonlinear activation layer.** Considering that an activation layer simply *rescales* the saliency weight matrices, *i.e.*,  $\mathbf{x}^{l+1} = g_l(\mathbf{x}^l) = h^l \circ \mathbf{x}^l$ , where  $\circ$  is the composition operator, we obtain  $\tilde{W}^l = h \circ \tilde{W}^{l+1}$ . Using the ReLU activation as a concrete example, we have  $h(\mathbf{x}^l) = \mathbb{1}\{\mathbf{x}^l \geq 0\}$ .

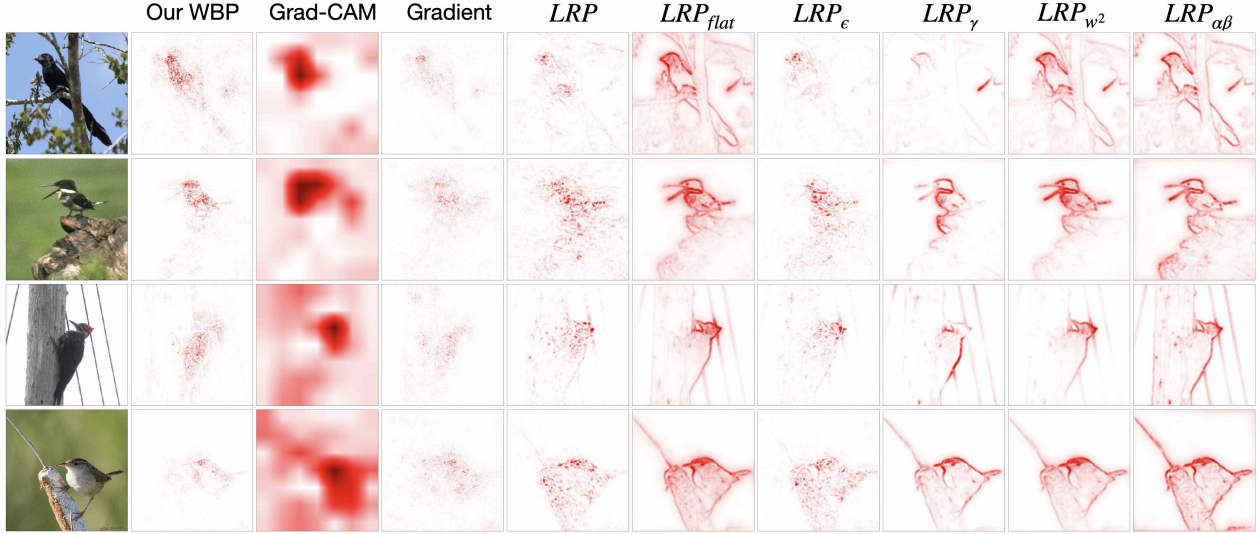


Figure 4: Comparisons of saliency maps on CUB dataset.

**Convolutional layer.** The convolution is a generalized form of linear mapping. In practice, convolutions can be expressed as tensor products of the form  $\tilde{W}^l = \tilde{W}^{l+1} \otimes [W^l]_{flip_{2,3}}^{T_{0,1}}$ , where  $W^l \in \mathbb{R}^{D_2 \times D_1 \times (2S+1) \times (2S+1)}$  is the convolution kernel,  $T_{0,1}$  is the transpose in dimensions 0 and 1 and  $flip_{2,3}$  is an exchange in dimensions 2 and 3. See the Appendix for details.

**Pooling and normalization layer.** Summarization and standardization are two other essential operations for the success of deep neural networks, achieved by pooling and batch normalization (BN) techniques, respectively. They too can be considered as special instantiations of linear operations. Here we summarize the two most popular operations in Table 1.

## 4. Experiments

To validate the utility of our approach, we consider a wide range of real-world datasets, and compare it to existing state-of-the-art solutions. All experiments are implemented in PyTorch. The source code is available from [https://github.com/author\\_name/PP1](https://github.com/author_name/PP1). Due to space limitations, details of the experimental setup and additional analyses are deferred to the Appendix.

**Datasets.** We present our findings on three representative datasets: (i) CUB [59], a natural image dataset with over 12k photos for classification of 200 bird species in the wild, heavily confounded by the background characteristics; (ii) GA [35], a new medical image dataset for the prediction of *geographic atrophy* (GA) using 3D *optical coherence tomography* (OCT) image volumes, characterized by small sample size (275 subjects) and highly heterogeneous (collected from 4 different facilities); and (iii)

LIDC-IDRI [34], a public medical dataset of 1,085 lung lesion CT images annotated by 4 radiologists. Detailed specifications are described in the Appendix.

**Baselines.** The following set of popular saliency mapping schemes are considered as comparators for the proposed approach: (i) Gradient: standard gradient-based salience mapping; (ii) Grad-CAM [49]: gradient-weighted class activation mapping; (iii) LRP [4]: layer-wise relevance propagation and its variants.

### 4.1. CUB: Bird classification in the wild

In this task we want to qualitatively and quantitatively compare the causal relevance of saliency maps generated by WBP and its competitors. In Figure 4 we show the saliency maps produced by different approaches for a VGG11 network trained on CUB (with 0.662 testing accuracy). Visually, gradient-based solutions (Grad and GradCAM) tend to yield overly dispersed maps, indicating a lack of specificity. Further, the chosen LRP models, which focus on either higher relevance points ( $LRP_e, LRP_w^2$ ) or positively weighted relevance points ( $LRP_\gamma, LRP_{\alpha\beta}$ ) [39], give very sharp saliency maps. However, these maps also heavily attend to the spurious background cues that presumably help with predictions. In contrast, WBP faithfully focuses the attention to the birds themselves. To quantitatively evaluate the causal relevance of competing saliency maps, we adopt the evaluation scheme proposed in [27], consisting of masking out the contributing saliency pixels and then calculating the reduction in prediction score. A larger reduction is considered better for accurately capturing the causal relevance. The results are summarized in Table 2, where we progressively remove the top- $k$  saliency points, with  $k = 100, 500, 1000, 5000, 10000$  ( $10000 \approx 6.6\%$  of all pix-

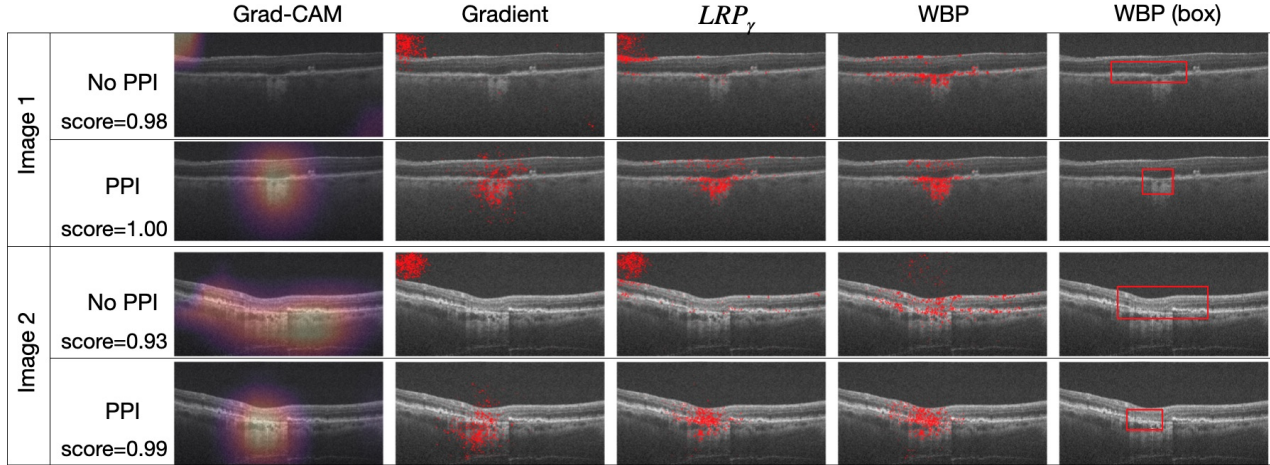


Figure 5: Saliency maps on GA dataset based on models trained with PPI and without PPI.

Table 2: Average prediction score reduction after removing the top  $k$  saliency pixels.

$k$	100	500	1000	5000	10000
$LRP$	-0.074	-0.162	-0.238	-0.447	-0.524
$LRP_{flat}$	-0.052	-0.131	-0.177	-0.341	-0.441
$LRP_\epsilon$	-0.065	-0.162	-0.226	-0.430	-0.516
$LRP_\gamma$	-0.051	-0.124	-0.174	-0.339	-0.422
$LRP_{w2}$	-0.052	-0.126	-0.174	-0.343	-0.436
$LRP_{\alpha\beta}$	-0.059	-0.141	-0.192	-0.353	-0.467
$Gradient$	-0.035	-0.167	-0.269	-0.494	-0.554
$Grad-CAM$	-0.031	-0.165	-0.283	-0.536	-0.616
<b>WBP</b>	<b>-0.263</b>	<b>-0.489</b>	<b>-0.576</b>	<b>-0.654</b>	<b>-0.662</b>

els), from the test input images. Our WBP consistently outperforms its counterparts, with its lead being most substantial in the low- $k$  regime. Notably, for large  $k$ , WBP removes nearly all predictive signal. This implies WBP specifically targets the causal features.

## 4.2. OCT-GA: Geographic Atrophy Classification

Next we seek to show how the proposed PPI handles the challenges of small sample size and heterogeneity in medical image datasets. In this experiment (with our new dataset, that we will make public), each OCT volume image consists of 100 scans, each of which being a  $512 \times 1000$  pixel image [5]. We use a multi-view CNN model [54] to process such 3D OCT inputs, and use it as our baseline solution (see the Appendix for details). We investigate how the different pairings of PPI and saliency mapping schemes (*i.e.*, Grad, GradCAM, LRP, WBP) affect performance. For WBP, we also tested the bounding box variant (see the Appendix for details). In Table 3, we see consistent performance gains in AUC score via incorporating PPI training (from 0.877 to 0.937), accompanied by the reductions in model vari-

Table 3: AUC results for GA prediction. We report means and standard deviations (SDs) from 5-fold cross-validation.

	<b>AUC</b>	<b>Mean</b>	<b>STD</b>
Multi-view CNN	0.877	0.040	
+PPI <sub>GradCAM</sub>	0.908	0.036	
+PPI <sub>WBP</sub>	0.925	0.023	
+PPI <sub>WBP(box)</sub>	<b>0.937</b>	<b>0.015</b>	

ation evaluated by the standard deviations of AUC from the five-fold cross-validation. The gains are most significant when using our WBP for saliency mapping. We further compare the saliency maps generated by these different combinations. We see that without the additional supervision from PPI, competing solutions like Grad, GradCAM and LRP sometimes yield non-sensible saliency maps (attending to image corners). Overall, PPI encourages more concentrated and less noisy saliency maps. Also, different PPI-based saliency maps agree with each other to a larger extent. Our findings are also verified by experts (co-authors, who are ophthalmologists specializing in GA) confirming that the PPI-based saliency maps are clinically relevant by focusing on retinal layers likely to contain abnormalities or lesions. These results underscore the practical value of the proposed proactive interventions.

**Cross-domain generalization.** Common to medical image applications is that training samples are usually integrated from a number of healthcare facilities (*i.e.*, domains), and that predictions are sometimes to be made on subjects at other facilities. Despite big efforts to standardize the image collection protocols, with different imaging systems operated by technicians with varying skills, apparent domain shifts are likely to compromise the cross-domain performance of these models. We show this phenomenon

Table 4: AUC results for GA prediction with or without PPI. We transfer the model trained on one site to others. Darker color represents better performance.

+PPI	A	B	C	D	Mean	STD
A	1.000	0.906	0.877	0.865	<b>0.912</b>	<b>0.061</b>
B	0.851	0.975	0.863	0.910	<b>0.900</b>	0.056
C	0.954	0.875	0.904	0.931	<b>0.916</b>	<b>0.034</b>
D	0.824	0.846	0.853	0.904	<b>0.857</b>	<b>0.034</b>
No PPI	A	B	C	D	Mean	STD
A	1.000	0.854	0.832	0.827	0.878	0.082
B	0.810	0.874	0.850	0.906	0.860	<b>0.040</b>
C	0.860	0.779	0.873	0.862	0.843	0.043
D	0.748	0.792	0.836	0.961	0.834	0.092

on the GA dataset in Table 4, where source samples are collected from four different hospitals in different health systems (A, B, C and D, see the Appendix for details). Each cell contains the AUC of the model trained on site X (row) and tested on site Y (column), with same-site predictions made on hold-out samples. A significant performance drop is observed for cross-domain predictions (off-diagonals) compared to in-domain predictions (diagonals). With the application of PPI, the performance gaps between in-domain and cross-domain predictions are considerably reduced. The overall accuracy gains of PPI further justify the utility of causally-inspired modeling. Notably, site D manifests strong spurious correlation that help in-domain prediction but degrades out-of-site generalization, which is partly resolved by the proposed PPI.

### 4.3. LIDC-IDRI: Lung Lesions Classification

To further examine the practical advantages of the proposed PPI in real-world applications, we benchmark its utility on LIDC-IDRI; a public lung CT scan dataset [3]. We followed the preprocessing steps outlined in [31] to prepare the data, and adopted the experimental setup from [48] to predict lesions. We use Inception-v3 [56] as our base model for both standard classification and PPI-enhanced training with various saliency mapping schemes. See the Appendix for details.

**Lesion classification.** We first compare PPI to other specialized SOTA network architectures. Table 5 summarizes AUC scores of Tensor Net-X [15], DenseNet [28], LoTeNet [48], Inception-v3 [56], as well as our Incep-

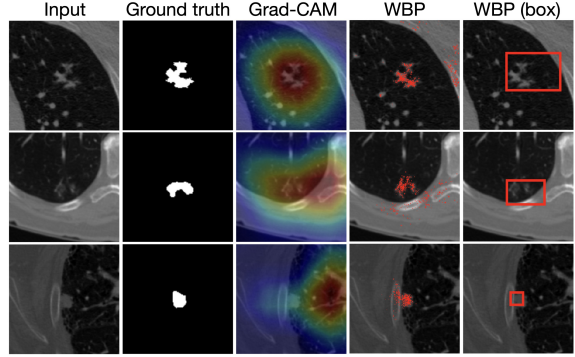


Figure 6: Saliency maps on LIDC-IDRI.

tion-v3 trained with and without  $PPI_{WBP}$ . The proposed  $PPI_{WBP(box)}$  leads the performance chart by a considerable margin, improving Inception-v3 from 0.92 to 0.94.

**Weakly-supervised image segmentation.** In Figure 6, we compare saliency maps generated by Grad-CAM, WBP, WBP (box) to the ground truth lesion masks from expert annotations. Note that we have only supplied patch-label labels during training, not the pixel-level expert segmentation masks, which constitute a challenging task of weakly-supervised image segmentation. In line with the observations from the GA experiment, our PPI-training enhanced WBP saliency maps are mostly consistent with the expert segmentations. Together with Table 5, Figure 6 demonstrates that the proposed PPI+WBP improves both the classification performance and model interpretability.

## 5. Conclusions

We have presented *Proactive Pseudo-Intervention* (PPI), a novel interpretable computer vision framework that combines saliency mapping, causal reasoning, synthetic intervention and contrastive learning. PPI couples saliency mapping with contrastive training by creating artificially intervened negative samples absent of causal features. To communicate model insights and facilitate causal-informed reasoning, we derived an architecture-agnostic saliency mapping scheme called *Weight Back Propagation* (WBP), which faithfully captures the causally-relevant pixels/features for model prediction. Visual inspection of the saliency maps show that WBP, especially when coupled with PPI, is more robust to spurious features compared to competing approaches. Tested on natural image and medical image datasets, empirical results verify the combination of PPI and WBP consistently delivers performance gains across a wide range of tasks relative to competing solutions, and the gains are most significant where the application is complicated by small sample size, data heterogeneity, or confounded with spurious correlations.

## References

- [1] Julius Adebayo, Justin Gilmer, Michael Muelly, Ian Goodfellow, Moritz Hardt, and Been Kim. Sanity checks for saliency maps. In *Advances in Neural Information Processing Systems*, pages 9505–9515, 2018. [1](#), [2](#)
- [2] Martin Arjovsky, Léon Bottou, Ishaan Gulrajani, and David Lopez-Paz. Invariant risk minimization. *arXiv preprint arXiv:1907.02893*, 2019. [1](#), [2](#), [3](#)
- [3] Samuel G Armato III, Geoffrey McLennan, Luc Bidaut, Michael F McNitt-Gray, Charles R Meyer, Anthony P Reeves, Binsheng Zhao, Denise R Aberle, Claudia I Henschke, Eric A Hoffman, et al. The lung image database consortium (lidc) and image database resource initiative (idri): a completed reference database of lung nodules on ct scans. *Medical physics*, 38(2):915–931, 2011. [8](#), [17](#)
- [4] Sebastian Bach, Alexander Binder, Grégoire Montavon, Frederick Klauschen, Klaus-Robert Müller, and Wojciech Samek. On pixel-wise explanations for non-linear classifier decisions by layer-wise relevance propagation. *PloS one*, 10(7):e0130140, 2015. [2](#), [6](#), [14](#)
- [5] David S Boyer, Ursula Schmidt-Erfurth, Menno van Lookeren Campagne, Erin C Henry, and Christopher Brittain. The pathophysiology of geographic atrophy secondary to age-related macular degeneration and the complement pathway as a therapeutic target. *Retina (Philadelphia, Pa.)*, 37(5):819, 2017. [7](#), [15](#)
- [6] Chun-Hao Chang, Elliot Creager, Anna Goldenberg, and David Duvenaud. Explaining image classifiers by counterfactual generation. In *International Conference on Learning Representations*, 2018. [2](#), [14](#), [15](#)
- [7] Aditya Chattpadhyay, Anirban Sarkar, Prantik Howlader, and Vineeth N Balasubramanian. Grad-cam++: Generalized gradient-based visual explanations for deep convolutional networks. In *2018 IEEE Winter Conference on Applications of Computer Vision (WACV)*, pages 839–847. IEEE, 2018. [14](#)
- [8] Chenyi Chen, Ari Seff, Alain Kornhauser, and Jianxiong Xiao. Deepdriving: Learning affordance for direct perception in autonomous driving. In *Proceedings of the IEEE International Conference on Computer Vision*, pages 2722–2730, 2015. [1](#)
- [9] Ting Chen, Simon Kornblith, Mohammad Norouzi, and Geoffrey Hinton. A simple framework for contrastive learning of visual representations. *arXiv preprint arXiv:2002.05709*, 2020. [3](#)
- [10] Piotr Dabkowski and Yarin Gal. Real time image saliency for black box classifiers. In *Advances in Neural Information Processing Systems*, pages 6967–6976, 2017. [1](#), [2](#), [14](#), [15](#)
- [11] Jia Deng, Wei Dong, Richard Socher, Li-Jia Li, Kai Li, and Li Fei-Fei. Imagenet: A large-scale hierarchical image database. In *2009 IEEE conference on computer vision and pattern recognition*, pages 248–255. Ieee, 2009. [1](#)
- [12] Li Deng. The mnist database of handwritten digit images for machine learning research [best of the web]. *IEEE Signal Processing Magazine*, 29(6):141–142, 2012. [1](#)
- [13] Amit Dhurandhar, Pin-Yu Chen, Ronny Luss, Chun-Chen Tu, Paishun Ting, Karthikeyan Shanmugam, and Payel Das. Explanations based on the missing: Towards contrastive explanations with pertinent negatives. In *Advances in Neural Information Processing Systems*, pages 592–603, 2018. [14](#)
- [14] Mengnan Du, Ninghao Liu, Qingquan Song, and Xia Hu. Towards explanation of dnn-based prediction with guided feature inversion. In *Proceedings of the 24th ACM SIGKDD International Conference on Knowledge Discovery & Data Mining*, pages 1358–1367, 2018. [14](#)
- [15] Stavros Efthymiou, Jack Hidary, and Stefan Leichenauer. Tensornetwork for machine learning. *arXiv preprint arXiv:1906.06329*, 2019. [8](#)
- [16] Dumitru Erhan, Yoshua Bengio, Aaron Courville, and Pascal Vincent. Visualizing higher-layer features of a deep network. *University of Montreal*, 1341(3):1, 2009. [14](#)
- [17] Ruth Fong, Mandala Patrick, and Andrea Vedaldi. Understanding deep networks via extremal perturbations and smooth masks. In *Proceedings of the IEEE International Conference on Computer Vision*, pages 2950–2958, 2019. [14](#)
- [18] Ruth C Fong and Andrea Vedaldi. Interpretable explanations of black boxes by meaningful perturbation. In *Proceedings of the IEEE International Conference on Computer Vision*, pages 3429–3437, 2017. [2](#), [14](#), [15](#)
- [19] Hiroshi Fukui, Tsubasa Hirakawa, Takayoshi Yamashita, and Hironobu Fujiyoshi. Attention branch network: Learning of attention mechanism for visual explanation. In *Proceedings of the IEEE Conference on Computer Vision and Pattern Recognition*, pages 10705–10714, 2019. [1](#), [2](#), [14](#), [15](#)

[20] AmirEmad Ghassami, Saber Salehkaleybar, Negar Kiyavash, and Kun Zhang. Learning causal structures using regression invariance. In *Advances in Neural Information Processing Systems*, pages 3011–3021, 2017. 3

[21] Ross Girshick, Jeff Donahue, Trevor Darrell, and Jitendra Malik. Rich feature hierarchies for accurate object detection and semantic segmentation. In *Proceedings of the IEEE conference on computer vision and pattern recognition*, pages 580–587, 2014. 1

[22] Yash Goyal, Ziyan Wu, Jan Ernst, Dhruv Batra, Devi Parikh, and Stefan Lee. Counterfactual visual explanations. In *ICML*, 2019. 2, 3, 14, 15

[23] Jean-Bastien Grill, Florian Strub, Florent Altché, Corentin Tallec, Pierre Richemond, Elena Buchatskaya, Carl Doersch, Bernardo Avila Pires, Zhaohan Guo, Mohammad Gheshlaghi Azar, et al. Bootstrap your own latent-a new approach to self-supervised learning. *Advances in Neural Information Processing Systems*, 33, 2020. 3

[24] Michael Gutmann and Aapo Hyvärinen. Noise-contrastive estimation: A new estimation principle for unnormalized statistical models. In *Proceedings of the Thirteenth International Conference on Artificial Intelligence and Statistics*, pages 297–304, 2010. 3

[25] Kaiming He, Haoqi Fan, Yuxin Wu, Saining Xie, and Ross Girshick. Momentum contrast for unsupervised visual representation learning. In *Proceedings of the IEEE/CVF Conference on Computer Vision and Pattern Recognition*, pages 9729–9738, 2020. 3

[26] Kaiming He, Xiangyu Zhang, Shaoqing Ren, and Jian Sun. Deep residual learning for image recognition. In *Proceedings of the IEEE conference on computer vision and pattern recognition*, pages 770–778, 2016. 3

[27] Sara Hooker, Dumitru Erhan, Pieter-Jan Kindermans, and Been Kim. A benchmark for interpretability methods in deep neural networks. In *Advances in Neural Information Processing Systems*, pages 9737–9748, 2019. 1, 2, 6

[28] Gao Huang, Zhuang Liu, Laurens Van Der Maaten, and Kilian Q Weinberger. Densely connected convolutional networks. In *Proceedings of the IEEE conference on computer vision and pattern recognition*, pages 4700–4708, 2017. 8

[29] Fredrik Johansson, Uri Shalit, and David Sontag. Learning representations for counterfactual inference. In *International conference on machine learning*, pages 3020–3029, 2016. 1

[30] Prannay Khosla, Piotr Teterwak, Chen Wang, Aaron Sarna, Yonglong Tian, Phillip Isola, Aaron Maschinot, Ce Liu, and Dilip Krishnan. Supervised contrastive learning. *arXiv preprint arXiv:2004.11362*, 2020. 3

[31] Simon Kohl, Bernardino Romera-Paredes, Clemens Meyer, Jeffrey De Fauw, Joseph R Ledsam, Klaus Maier-Hein, SM Ali Eslami, Danilo Jimenez Rezende, and Olaf Ronneberger. A probabilistic u-net for segmentation of ambiguous images. In *Advances in Neural Information Processing Systems*, pages 6965–6975, 2018. 8, 17

[32] Alex Krizhevsky, Geoffrey Hinton, et al. Learning multiple layers of features from tiny images. *Master’s thesis, University of Tront*, 2009. 1

[33] Alex Krizhevsky, Ilya Sutskever, and Geoffrey E Hinton. Imagenet classification with deep convolutional neural networks. *Communications of the ACM*, 60(6):84–90, 2017. 1

[34] Curtis P Langlotz, Bibb Allen, Bradley J Erickson, Jayashree Kalpathy-Cramer, Keith Bigelow, Tessa S Cook, Adam E Flanders, Matthew P Lungren, David S Mendelson, Jeffrey D Rudie, et al. A roadmap for foundational research on artificial intelligence in medical imaging: from the 2018 nih/rsna/acr/the academy workshop. *Radiology*, 291(3):781–791, 2019. 6

[35] Jessica N Leuschen, Stefanie G Schuman, Katrina P Winter, Michelle N McCall, Wai T Wong, Emily Y Chew, Thomas Hwang, Sunil Srivastava, Neeru Sarin, Traci Clemons, et al. Spectral-domain optical coherence tomography characteristics of intermediate age-related macular degeneration. *Ophthalmology*, 120(1):140–150, 2013. 6, 15

[36] Kunpeng Li, Ziyan Wu, Kuan-Chuan Peng, Jan Ernst, and Yun Fu. Tell me where to look: Guided attention inference network. In *Proceedings of the IEEE Conference on Computer Vision and Pattern Recognition*, pages 9215–9223, 2018. 14

[37] Aravindh Mahendran and Andrea Vedaldi. Salient de-convolutional networks. In *European Conference on Computer Vision*, pages 120–135. Springer, 2016. 14

[38] Grégoire Montavon. Gradient-based vs. propagation-based explanations: an axiomatic comparison. In *Explainable AI: Interpreting, Explaining and Visualizing Deep Learning*, pages 253–265. Springer, 2019. 14

[39] Grégoire Montavon, Alexander Binder, Sebastian Lapuschkin, Wojciech Samek, and Klaus-Robert Müller. Layer-wise relevance propagation: an overview. In *Explainable AI: interpreting, explaining and visualizing deep learning*, pages 193–209. Springer, 2019. [6](#), [14](#)

[40] Aaron van den Oord, Yazhe Li, and Oriol Vinyals. Representation learning with contrastive predictive coding. *arXiv preprint arXiv:1807.03748*, 2018. [3](#)

[41] Matthew O’Shaughnessy, Gregory Canal, Marissa Connor, Christopher Rozell, and Mark Davenport. Generative causal explanations of black-box classifiers. *Advances in Neural Information Processing Systems*, 33, 2020. [3](#), [14](#)

[42] Judea Pearl. *Causality*. Cambridge university press, 2009. [3](#)

[43] Vitali Petsiuk, Abir Das, and Kate Saenko. Rise: Randomized input sampling for explanation of black-box models. *arXiv preprint arXiv:1806.07421*, 2018. [14](#)

[44] Sylvestre-Alvise Rebuffi, Ruth Fong, Xu Ji, and Andrea Vedaldi. There and back again: Revisiting back-propagation saliency methods. In *Proceedings of the IEEE/CVF Conference on Computer Vision and Pattern Recognition*, pages 8839–8848, 2020. [1](#), [2](#)

[45] Marco Tulio Ribeiro, Sameer Singh, and Carlos Guestrin. ” why should i trust you?” explaining the predictions of any classifier. In *Proceedings of the 22nd ACM SIGKDD international conference on knowledge discovery and data mining*, pages 1135–1144, 2016. [14](#)

[46] Paul Sajda. Machine learning for detection and diagnosis of disease. *Annu. Rev. Biomed. Eng.*, 8:537–565, 2006. [1](#)

[47] Bernhard Schölkopf. Causality for machine learning. *arXiv preprint arXiv:1911.10500*, 2019. [3](#)

[48] Raghavendra Selvan and Erik B Dam. Tensor networks for medical image classification. In *Medical Imaging with Deep Learning*, 2020. [8](#), [17](#)

[49] Ramprasaath R Selvaraju, Michael Cogswell, Abhishek Das, Ramakrishna Vedantam, Devi Parikh, and Dhruv Batra. Grad-cam: Visual explanations from deep networks via gradient-based localization. In *Proceedings of the IEEE International Conference on Computer Vision*, pages 618–626, 2017. [2](#), [6](#), [14](#)

[50] Dasom Seo, Kanghan Oh, and Il-Seok Oh. Regional multi-scale approach for visually pleasing explanations of deep neural networks. *IEEE Access*, 8:8572–8582, 2019. [14](#)

[51] Avanti Shrikumar, Peyton Greenside, and Anshul Kundaje. Learning important features through propagating activation differences. In *International Conference on Machine Learning*, pages 3145–3153, 2017. [2](#), [14](#)

[52] Karen Simonyan, Andrea Vedaldi, and Andrew Zisserman. Deep inside convolutional networks: Visualising image classification models and saliency maps. *arXiv preprint arXiv:1312.6034*, 2013. [1](#)

[53] Karen Simonyan and Andrew Zisserman. Very deep convolutional networks for large-scale image recognition. *arXiv preprint arXiv:1409.1556*, 2014. [3](#)

[54] Hang Su, Subhransu Maji, Evangelos Kalogerakis, and Erik Learned-Miller. Multi-view convolutional neural networks for 3d shape recognition. In *Proceedings of the IEEE international conference on computer vision*, pages 945–953, 2015. [7](#), [15](#)

[55] Raphael Suter, Djordje Miladinovic, Bernhard Schölkopf, and Stefan Bauer. Robustly disentangled causal mechanisms: Validating deep representations for interventional robustness. In *International Conference on Machine Learning*, pages 6056–6065. PMLR, 2019. [3](#)

[56] Christian Szegedy, Vincent Vanhoucke, Sergey Ioffe, Jon Shlens, and Zbigniew Wojna. Rethinking the inception architecture for computer vision. In *Proceedings of the IEEE conference on computer vision and pattern recognition*, pages 2818–2826, 2016. [3](#), [8](#), [17](#)

[57] Yonglong Tian, Dilip Krishnan, and Phillip Isola. Contrastive multiview coding. *arXiv preprint arXiv:1906.05849*, 2019. [3](#)

[58] Jorg Wagner, Jan Mathias Kohler, Tobias Gindel, Leon Hetzel, Jakob Thaddaus Wiedemer, and Sven Behnke. Interpretable and fine-grained visual explanations for convolutional neural networks. In *Proceedings of the IEEE Conference on Computer Vision and Pattern Recognition*, pages 9097–9107, 2019. [2](#), [14](#)

[59] C. Wah, S. Branson, P. Welinder, P. Perona, and S. Belongie. The Caltech-UCSD Birds-200-2011 Dataset. Technical Report CNS-TR-2011-001, California Institute of Technology, 2011. [6](#)

- [60] Haohan Wang, Zexue He, Zachary C Lipton, and Eric P Xing. Learning robust representations by projecting superficial statistics out. In *International Conference on Learning Representations*, 2019. 3
- [61] Lezi Wang, Ziyuan Wu, Srikrishna Karanam, Kuan-Chuan Peng, Rajat Vikram Singh, Bo Liu, and Dimitris N Metaxas. Sharpen focus: Learning with attention separability and consistency. In *Proceedings of the IEEE International Conference on Computer Vision*, pages 512–521, 2019. 1, 2, 15
- [62] Tan Wang, Jianqiang Huang, Hanwang Zhang, and Qianru Sun. Visual commonsense representation learning via causal inference. In *Proceedings of the IEEE/CVF Conference on Computer Vision and Pattern Recognition Workshops*, pages 378–379, 2020. 1
- [63] Matthew D Zeiler and Rob Fergus. Visualizing and understanding convolutional networks. In *European conference on computer vision*, pages 818–833. Springer, 2014. 14
- [64] Cheng Zhang, Kun Zhang, and Yingzhen Li. A causal view on robustness of neural networks. *arXiv preprint arXiv:2005.01095*, 2020. 3
- [65] Yitian Zhao, Yalin Zheng, Yifan Zhao, Yonghuai Liu, Zhili Chen, Peng Liu, and Jiang Liu. Uniqueness-driven saliency analysis for automated lesion detection with applications to retinal diseases. In *International Conference on Medical Image Computing and Computer-Assisted Intervention*, pages 109–118. Springer, 2018. 1
- [66] Bolei Zhou, Aditya Khosla, Agata Lapedriza, Aude Oliva, and Antonio Torralba. Learning deep features for discriminative localization. In *Proceedings of the IEEE conference on computer vision and pattern recognition*, pages 2921–2929, 2016. 2

## A. Derivation of Convolutional Weight Back-propagation

Let's denote the input variable as  $I \in \mathbb{R}^{H \times W}$ , the convolutional filter weight as  $W \in \mathbb{R}^{(2S+1) \times (2S+1)}$ , the output

$$O = I \otimes W \quad (11)$$

$$O_{i,j} = \sum_{i'=-S}^S \sum_{j'=-S}^S I_{i+i',j+j'} W_{i'+S,j'+S} \quad (12)$$

$$\sum_i \sum_j O_{i,j} \tilde{W}_{i,j} = \sum_i \sum_j \sum_{i'=-S}^S \sum_{j'=-S}^S I_{i+i',j+j'} W_{i'+S,j'+S} \tilde{W}_{i,j} \quad (13)$$

$$\sum_i \sum_j O_{i,j} \tilde{W}_{i,j} = \sum_i \sum_j I_{i,j} \sum_{i'=-S}^S \sum_{j'=-S}^S \tilde{W}_{i+i',j+j'} W_{-i'+S,-j'+S} \quad (14)$$

$$\sum_i \sum_j O_{i,j} \tilde{W}_{i,j} = \sum_i \sum_j I_{i,j} (\tilde{W} \otimes [W]_{flip_{i,j}})_{i,j} \quad (15)$$

Hence the weight backpropagate through a convolutional layer is  $\tilde{W}^l = \tilde{W}^{l+1} \otimes [W^l]_{flip}$ . For the 3D cases,  $I^l \in \mathbb{R}^{D_1 \times H \times W}$ , the weight back propagates to  $O^l$  is  $\tilde{W}^{l+1} \in \mathbb{R}^{D_2 \times H \times W}$  and the convolutional weight is  $W^l \in \mathbb{R}^{D_2 \times D_1 \times (2S+1) \times (2S+1)}$ . To match the depth of  $\tilde{W}^{l+1}$ , the  $W^l$  is transposed in the first two dimensions. So  $\tilde{W}^l = \tilde{W}^{l+1} \otimes [W^l]_{flip_{2,3}}^{T_{0,1}}$ . If the convolutional layer is downsizing the input variable (*i.e.*, strides), the  $\tilde{W}_{ijk}^{l+1}$  is padded with zeros around the weights (left, right, up, and down) to display the input elements that the convolutional filter strides over. The number of padding zeros is equal to the number of strides minus 1.

## B. Details on Causal Masking

In this work, we consider three types of causal masking: (*i*) the point-wise soft causal masking defined by Equation (2) in the main text, (*ii*) hard masking, and (*iii*) box masking. For the hard masking, for each image, we keep points with WBP weight larger than  $k$  times of the standard deviation of WBP weights of the whole image. We test  $k$  from 1 to 7 and achieve similar results. As the model performs slightly better when  $k = 7$ , we set  $k$  as 7 for all experiments. For the box masking, we use the center of mass for these kept points as the center to draw a box. The height and width of this box is defined as  $center_{h/w} \pm 1.2std_{h/w}$ . In this way at least 90% of filtered points are contained in the box. For the soft masking, we set  $\omega$  to 100 and  $\sigma$  to 0.25. We have also experimented with image-adaptive thresholds instead of a fixed  $\sigma$  for all inputs, *i.e.*, set the threshold as mean value plus  $k$  times of the standard deviation of WBP

variable as  $O \in \mathbb{R}^{H \times W}$ , and the weight backpropagate to  $O$  as  $\hat{W} \in \mathbb{R}^{H \times W}$ . We omit the bias here because it does not directly interact with the input variables. We denote  $\otimes$  as the convolutional operator. We have the following equations.

$$O = I \otimes W \quad (11)$$

$$O_{i,j} = \sum_{i'=-S}^S \sum_{j'=-S}^S I_{i+i',j+j'} W_{i'+S,j'+S} \quad (12)$$

$$\sum_i \sum_j O_{i,j} \tilde{W}_{i,j} = \sum_i \sum_j \sum_{i'=-S}^S \sum_{j'=-S}^S I_{i+i',j+j'} W_{i'+S,j'+S} \tilde{W}_{i,j} \quad (13)$$

$$\sum_i \sum_j O_{i,j} \tilde{W}_{i,j} = \sum_i \sum_j I_{i,j} \sum_{i'=-S}^S \sum_{j'=-S}^S \tilde{W}_{i+i',j+j'} W_{-i'+S,-j'+S} \quad (14)$$

$$\sum_i \sum_j O_{i,j} \tilde{W}_{i,j} = \sum_i \sum_j I_{i,j} (\tilde{W} \otimes [W]_{flip_{i,j}})_{i,j} \quad (15)$$

weights of the whole image. The experiment comparison of these masking methods mention above is conducted on LIDC dataset. We repeat the experiments a few times and the results are consistent.

Table 6: AUC on LIDC from different causal masking methods

Models	AUC
WBP-soft (fixed $\sigma$ )	0.931
WBP-soft (adaptive $\sigma$ )	0.941
WBP-hard	0.935
WBP-box	<b>0.941</b>

## C. Related Work

In this work, we propose a contrastive causal representation learning strategy, *i.e.*, Proactive Pseudo-Intervention (PPI), that leverages proactive interventions to identify causally-relevant image features. This approach is complemented with a novel causal salience map visualization module, *i.e.*, Weight Back Propagation (WBP), that identifies important pixels in the raw input image, which greatly facilitates interpretability of predictions.

Prior related works will be discussed in this section. Compared with alternative post-hot saliency mapping methods, WBP outperforms these methods as both a standalone causal saliency map and a trainable model for model interpretation. Compared with other trainable interpretation

models, the proposed PPI+WBP improves both model performance and model interpretations.

### C.1. Post-hoc Saliency Maps

We compare WBP with other post-hoc saliency mapping methods to show why WBP is able to target the causal features, and generate more succinct and reliable saliency maps.

**Perturbation Based Methods** These methods make perturbations to individual inputs or neurons and monitor the impact on output neurons in the network. [63] occludes different segments of an input image and visualized the change in the activations of subsequent layers. Several methods follow a similar idea, but use other importance measures or occlusion strategies [43, 45, 50]. More complicated work generates an explanation by optimizing for a perturbed version of the image [18, 17, 10, 14]. [58] proposes a new adversarial defense technique which filters gradients during optimization to achieve fine-grained explanation. However, such perturbation based methods are computationally intensive and involve sophisticated model designs, which make it extremely hard to be integrated with other advance learning strategies.

**Backpropagation Based Methods** Backpropagation based methods (BBM) propagate an importance signal from an output neuron backwards through the layers to the input. These methods are usually fast to compute and produce fine-grained importance/relevancy maps. WBP is one of such method.

The pioneer methods in this category backpropagate a gradient to the image, and branches of studies extend this work by manipulating the gradient. These methods are discussed and compared in [37, 16]. However, these maps are generally less concentrated [10, 18] and less interpretable. Other BBMs such as Layer-wise Relevance Propagation [4], DeepLift [51] employ top-down relevancy propagation rules. DeepLift is sensitive to the reference inputs, which needs more human efforts and background knowledge to produce appealing saliency maps. The nature of depending on reference inputs limits its ability on model diagnosis and coupled with learning strategies to continuously improving models’ performance. LRP decomposes the relevance,  $R$ , from a neuron,  $k$ , in the upper layer to every connected neurons,  $j$ , in the lower layer. The decomposition is distributed through gradients under the suggested implementation [39]. Our experiments on GA and CUB datasets show that vanilla LRP performs similar to gradient based methods, which is also demonstrated in [38]. The variants of LRP use complex rules to prioritize positive or large relevance, making the saliency map visually appealing to human. However, our experiments demonstrate the unfaithfulness of LRP and its variants as they highlight spuriously correlated features (boarderlines and backgrounds).

By contrast, our WBP backpropagates the the weights of through layers to compute the contributions of each input pixel, which is truly faithful to the model, and WBP tends to highlight the target objects themselves rather than the background. At the same time, the simplicity and efficiency makes WBP easily work with other advanced learning strategies for both model diagnosis and improvements during training.

Table 7: A list of commonly used LRP rules.[39]

Rules	Formula
$LRP$	$R_j = \sum_k \frac{a_j w_{jk}}{\sum_{0,j} a_j w_{jk}} R_k$
$LRP_\epsilon$	$R_j = \sum_k \frac{a_j w_{jk}}{\epsilon + \sum_{0,j} a_j w_{jk}} R_k$
$LRP_\gamma$	$R_j = \sum_k \frac{a_j (w_{jk} + \gamma w_{jk}^+)}{\sum_{0,j} a_j (w_{jk} + \gamma w_{jk}^+)} R_k$
$LRP_{\alpha\beta}$	$R_j = \sum_k (\alpha \frac{(a_j w_{jk})^+}{\sum_{0,j} (a_j w_{jk})^+} - \beta \frac{(a_j w_{jk})^-}{\sum_{0,j} (a_j w_{jk})^-}) R_k$
$LRP_{flat}$	$R_j = \sum_k \frac{1}{\sum_j 1} R_k$
$LRP_{w^2}$	$R_j = \sum_j \frac{w_{ij}^2}{\sum_i w_{ij}^2} R_j$
$LRP_{Z^\beta}$	$R_j = \sum_j \frac{x_i w_{ij} - l_i w_{ij}^+ - h_i w_{ij}^-}{\sum_i x_i w_{ij} - l_i w_{ij}^+ - h_i w_{ij}^-} R_j$

**Activation Based Methods** Methods under this category (such as CAM, Grad-CAM, guided Grad-CAM, Grad-CAM++) use a linear combination of class activation maps from convolutional layers to derive a saliency map. The main difference between them is how the linear combination weights are computed.

The generation of saliency maps is simple and these methods can be coupled with advanced training strategies to improve training [36]. However, they fail at visualizing fine-grained evidence, which is particularly important in explaining medical classification models. Additionally, it is not guaranteed that the resulting explanations are faithful and reflect the decision making process of the model [14, 49, 58]. Grad-CAM++ [7] proposes to introduce higher-order derivatives to capture pixel-level importance, while its high computational cost in calculating the second- and third-order derivatives makes it impractical for training purposes.

### C.2. Interpretable Models

Unlike the *post hoc* saliency map generation described above, an alternative approach is to train a separate module to explicitly produce model explanations [19, 22, 6, 18, 51]. Such *post hoc* causal explanations can be generated with black-box classifiers based on a learned low-dimensional representation of the data [41]. Related to our work is adversarial-based visual explanation method is developed in [58], highlighting the key features in the input image for a specific prediction. Contrastive explanations are produced in [13] to justify the predictions from a deep neural network.

Also in [22] the authors generate counterfactual visual explanations that highlight what and how regions of an image would need to change in order for the model to predict a *distractor* class  $c'$  instead of the predicted class  $c$ . The main differences to our construction are two fold: (i) they rely on a separate module to be trained, and (ii) these approaches only produce explanations, but such explanations are not exploited to provide feedback for model improvement.

Striking the goal of both good explanation and good performance is more challenging. One promising direction is to inject model-dependent perturbations to the input images as strategic augmentations [18, 10, 6]. In such examples, parts of the image have been masked and replaced with various references such as mean pixel values, blurred image regions, random noise, outputs of generative models, *etc*. However, these pixel-level perturbations are very costly and difficult to craft. [61] propose new learning objectives for attention separability and cross-layer consistency, which result in improved attention discriminability and reduced visual confusion. However, it generates heat-map style attention maps, which fail in fine-resolution model explanations which is important in medical related tasks. In [19] an additional attention branch is learned to generate attention map, and then applies the attention map to the original image or feature map; they achieve compelling attention maps on natural images. However, as the attention maps are not derived directly from the classification model, there is no guarantee for their faithfulness. Further, having an additional attention network results in increased network size, which raises concerns for the risk of over-fitting, particularly on datasets with a limited sample size.

## D. CUB Experiment Details

### D.1. CUB dataset descriptions and experiemnt settings

CUB has 11,788 images of 200 bird species. To train a VGG11 network, we use 8,190 training images and validate the model on 2,311 validation images, with the accuracy are reported on 1227 testing images. The network is trained for 100 epochs with a learning rate decay of 0.1 every 30 epochs. The batch size is 32. The optimizer is a SGD with initial learning rate at 0.01.

### D.2. Classification performance improvement with PPI

We compare classification performances among model trained with different objections. The baseline is VGG11 classification without PPI. Three different saliency mapping methods are tested within our PPI framework: LRP, Grad-CAM, and WBP. Top 1000 points in all saliency maps are used to generate the soft mask so the comparison is fair. During training, since only a small portion of points are

used to generate the mask, the contribution from  $L_{con}$  is about 100 times smaller than other losses. To fix this imbalance, the  $L_{con}$  is weighted 100 $\times$  more after the first 20 epochs. The results are shown in Table 8.

Table 8: Accuracy on CUB

Models	Accuracy
VGG 11	0.662
+PPI <sub>LRP</sub>	0.680
+PPI <sub>Grad-CAM</sub>	0.683
+PPI <sub>WBP</sub>	<b>0.696</b>

## E. Geographic Atrophy (GA) Experiment Details

### E.1. GA dataset descriptions

Our GA dataset is derived from the A2A SD-OCT Study (<http://ClinicalTrials.gov> identifier NCT00734487), which was an ancillary observational prospective study of a subset of eyes from the AREDS2 conducted at four sites (National Eye Institute, Duke Eye Center, Emory Eye Center, and Devers Eye Institute) [35]. In this experiment (with our new dataset, that we will make public), each OCT volume image consists of 100 scans, each of which being a 512  $\times$  1000 pixel image [5]. 1,085 OCT images are collected from 275 subjects during 5 years. An example of 3D OCT images is shown in Figure. 7.

### E.2. Image differences between 4 sites

Images in GA dataset are collected from 4 different sites, hereafter denoted as A, B, C, and D respectively. There are 315 images (101 positive samples) from site A, 334 images (73 positive samples) from site B, 260 images (131 positive samples) from site A, and 176 images (59 positive samples) from site D. We show typical example images from 4 sites separately in Figure. 8. As the dataset is collected during 7 years, some images in site D are of smaller image size as they are sampled with different type of machine. We paddle these images by repeating the left and right areas, as show in the right bottom example.

### E.3. Multi-view CNN Variation

We use a variant of the multi-view CNN model [54] to process the 3D OCT inputs, and use it as our baseline solution. The architecture of this model is outlined in Figure 9. For each slice, the model feed it into a CNN network, and get the feature  $f_i$  of slice  $i$  ( $f_i = CNN(x_i)$ ), followed by a fully connected layer and a Sigmoid activation to get a probability score  $p_i = sigmoid(FC_1(f_i))$ . We observe that slices in different slices contributes differently to the

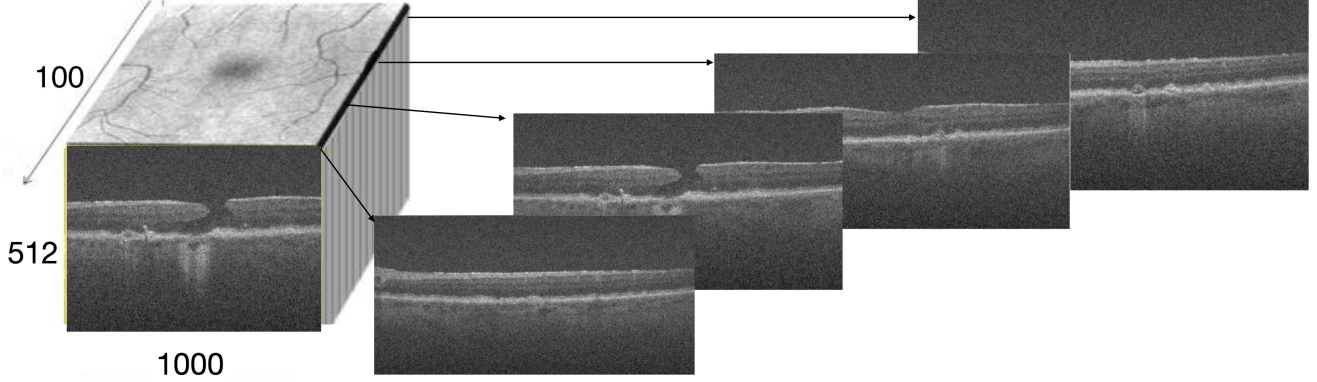


Figure 7: Illustration of a 3D OCT image example.

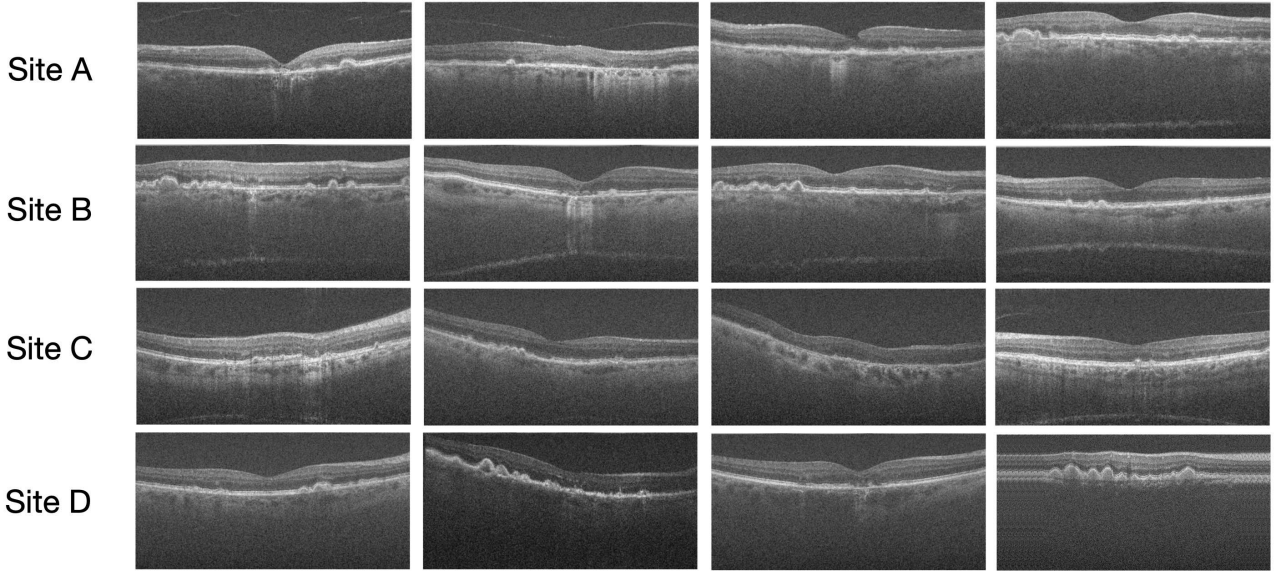


Figure 8: OCT slice examples from 4 site.

identification of GA, which motivates us to implement a location-aware view pooling, illustrated in the right part of Fig. 9. Each slice is assigned to a position id, ranging from 1 to 100. The model first uses an embedding layer to embed the position id to a six dimension position feature vector  $e_i$ . Then, we combine the feature vector  $f_i$  extracted from the slice image with the corresponding  $e_i$  together. The combined feature vector is fed into a fully connected layer to get the logit score  $a_i$ .

$$a_i = FC_2([f_i, e_i]) \quad (16)$$

To reduce computational burden during training, we randomly sample 10 out of the 100 slices (with an abuse of notation, denoted by  $a_1, a_2, \dots, a_{10}$ ) and send them into a Softmax function to get the attention weights for the 10

sampled slices, using the following equation

$$w_i = \frac{\exp((ReLU(a_i) + \delta)/\tau)}{\sum_{k=1}^{10} \exp((ReLU(a_k) + \delta)/\tau)} \quad (17)$$

Here  $\delta$  is a trainable bias term parameter, initialized to a high value to stabilize the training, and gradually attenuated to a small number during training.  $\tau$  is the temperature parameter, which is set to a small value to sharpen the attention weight, which helps us to find out the most important slices for GA diagnosis. The get final predicted probability of GA (GA score) for an image  $x$  at inference time, we compute the weighted summation of the probabilities  $w_i$  of all 100 slices  $GA = \sum_i w_i p_i$ .

#### E.4. Experiment settings

The CNN network is an Inception\_v3, which is pre-trained on ImageNet. For training all models, we use the

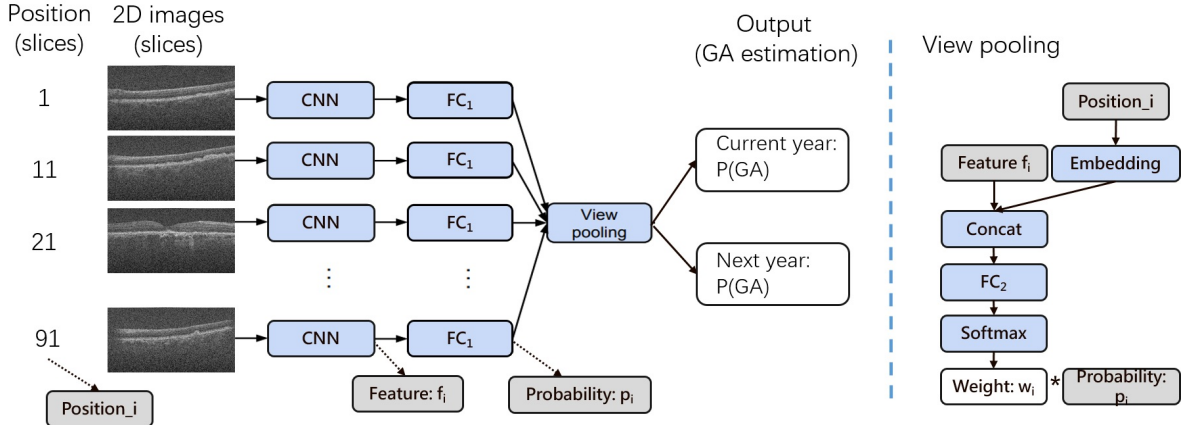


Figure 9: Illustration of multi-view CNN based 3D OCT image classification model.

Adam optimizer with a learning rate of  $5 \times 10^{-5}$  with a learning rate decay of 0.5 every 10 epochs for the pre-trained CNN network, and the Adam optimizer with a learning rate of  $5 \times 10^{-3}$  with a learning rate decay of 0.2 every 10 epochs for the other layers in the model. We train the model for 30 epochs with a batch size of 2 because of the large size of 3D OCT images. Random horizontal flips, and Gaussian noise are used for data augmentations during training.

## F. LIDC Experiment Details

### F.1. LIDC dataset description and experiment settings

We also test the proposed method on a public medical CT scan dataset LIDC-IDRI [3]. We follow the settings in [31, 48] that crops the original images into  $128 \times 128$  patches centered on a lesion for which at least one radiologist has annotated. In our experiment, we focus on the classification task of predicting the presence of a lesions, which is consistent with the setup of [48]. There are four radiologists annotate each patch with both lesion label and lesion mask. A patch in the dataset is labeled as positive if more than two (*i.e.*  $\geq 3$ ) radiologists have annotated presence of a lesion, otherwise negative. The ground-truth mask is the pixel-level union set of the four masks. We use Inception-v3 [56] as our base model for both standard classification and PPI-enhanced training with various saliency mapping schemes. To match the receptive field of an Inception-v3 model, we resize the input patches to  $299 \times 299$ . For training all models, we use the Adam optimizer with a learning rate of  $10^{-4}$  with a learning rate decay of 0.3 every 10 epochs after epoch 50, and a batch size of 64. Random horizontal flips, vertical flips and rotations within 20 degrees are used for data augmentations during training. As all patches are centered on a lesion, we randomly shift masks used in

the positive contrast to reduce overlaps between masks of positive and negative contrasts.

## G. Potential Application Discussion

Both quantitative and qualitative results show that PPI+WBP can not only improve the model performance, but also earn trusts from doctors, which is essential to accelerate clinical deployments of deep learning methods.

It is very time consuming and easy to miss small focuses for radiologists to review volume CT scans. The fine-grained saliency maps generated by PPI+WBP can potentially assist radiologist to diagnosis scan images by highlighting disease casual related areas.

When the classification model outperforms human experts, fine-grained casual saliency maps generated by PPI+WBP can potentially inspire doctors to discover disease related bio-markers, which in turn improves performance of human experts.

## H. Additional Saliency Map Comparisons

Extra saliency map comparisons on CUB, GA, and LIDC are shown in Figure. 10, 11, and 12. In Figure. 11 and 12, we observe that without the additional supervision from PPI, competing solutions like Grad, LRP sometimes yield non-sensible saliency maps (attending to image corners), and GradCAM yields saliency maps in coarse-grained. Overall, PPI encourages more concentrated and less noisy saliency maps. Also, different PPI-based saliency maps agree with each other to a larger extent.

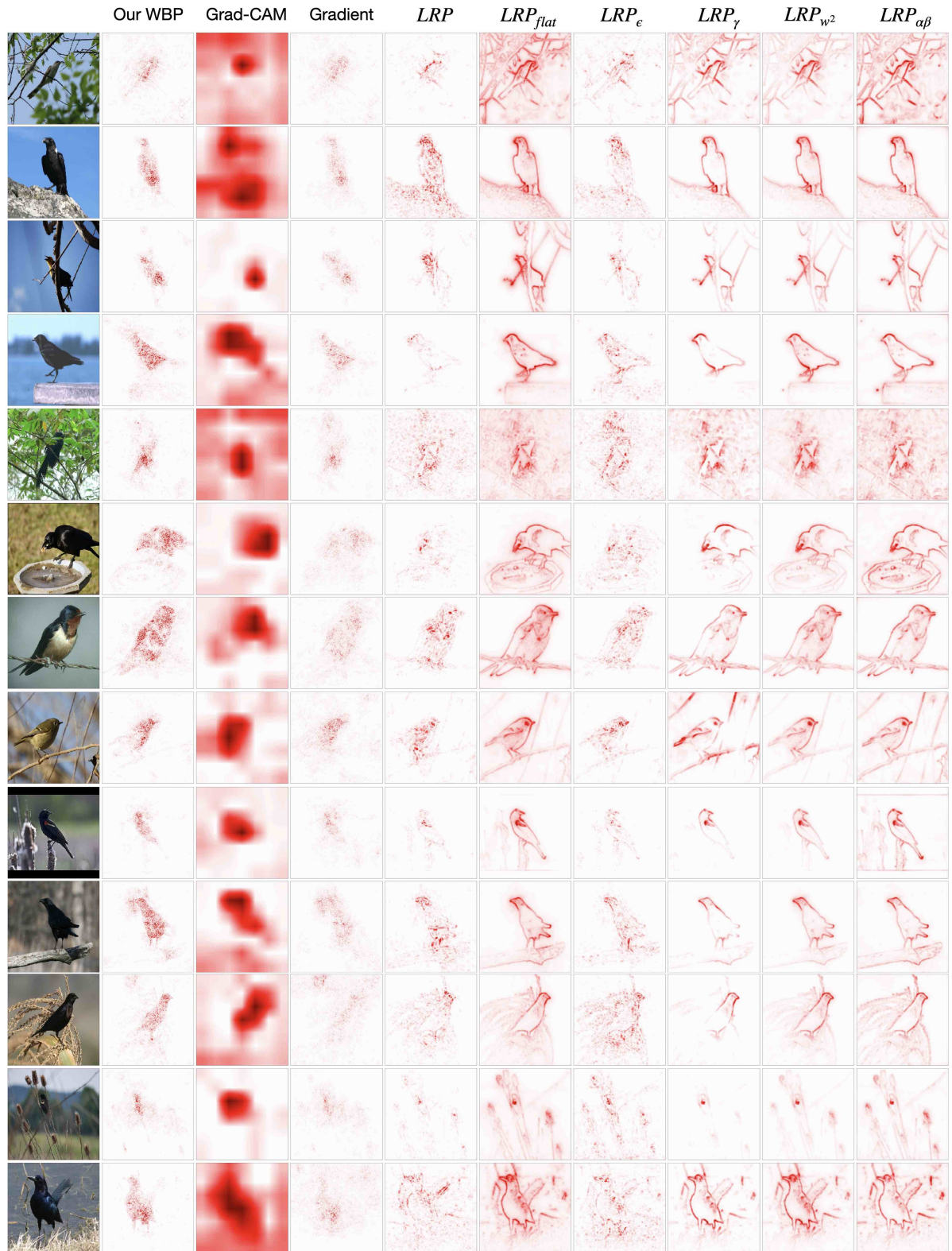


Figure 10: More comparisons of saliency maps on CUB dataset.

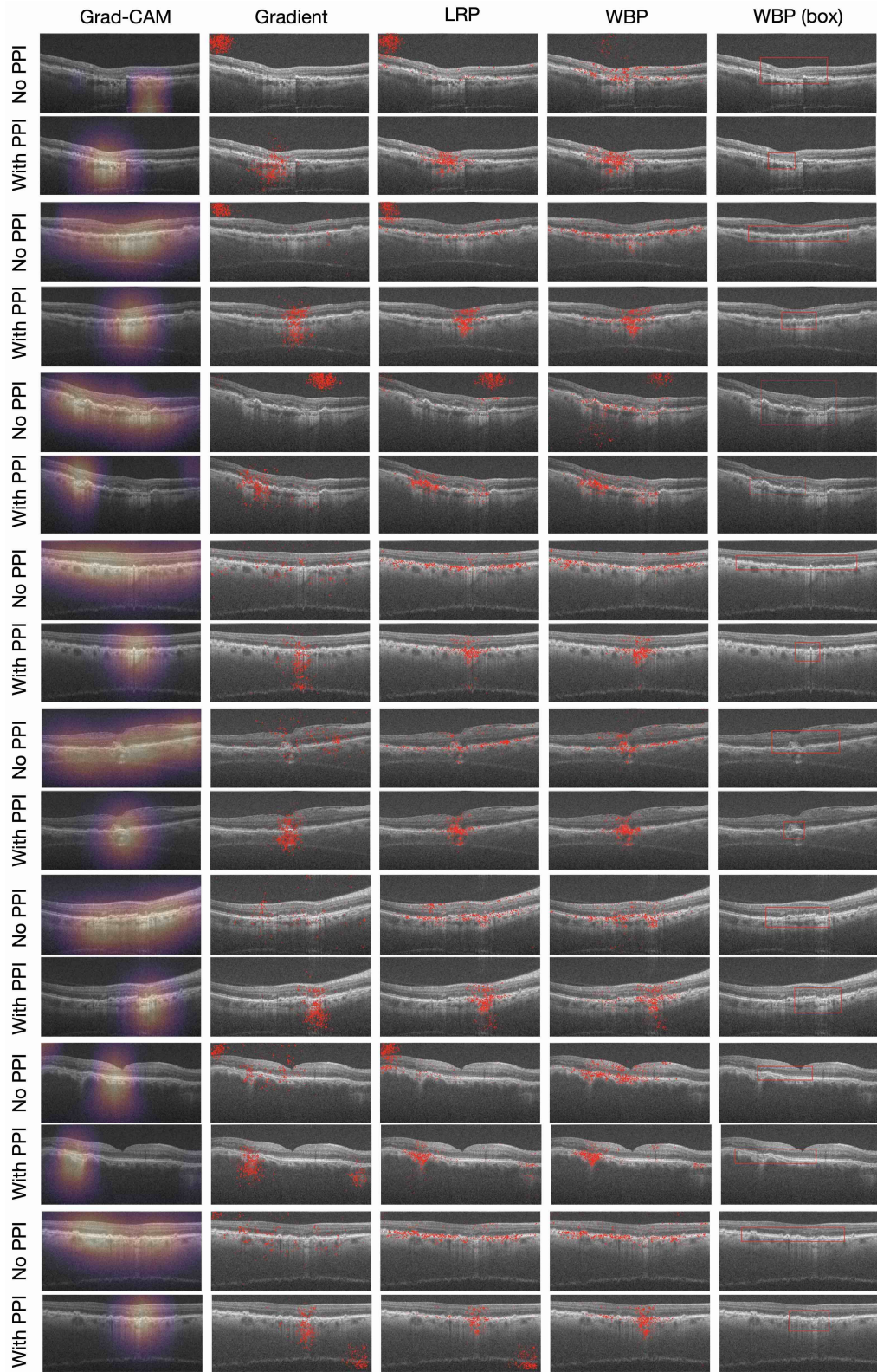


Figure 11: Comparison examples of saliency maps on GA dataset based on model trained with and without PPI. PPI encourages more concentrated and less noisy saliency maps.

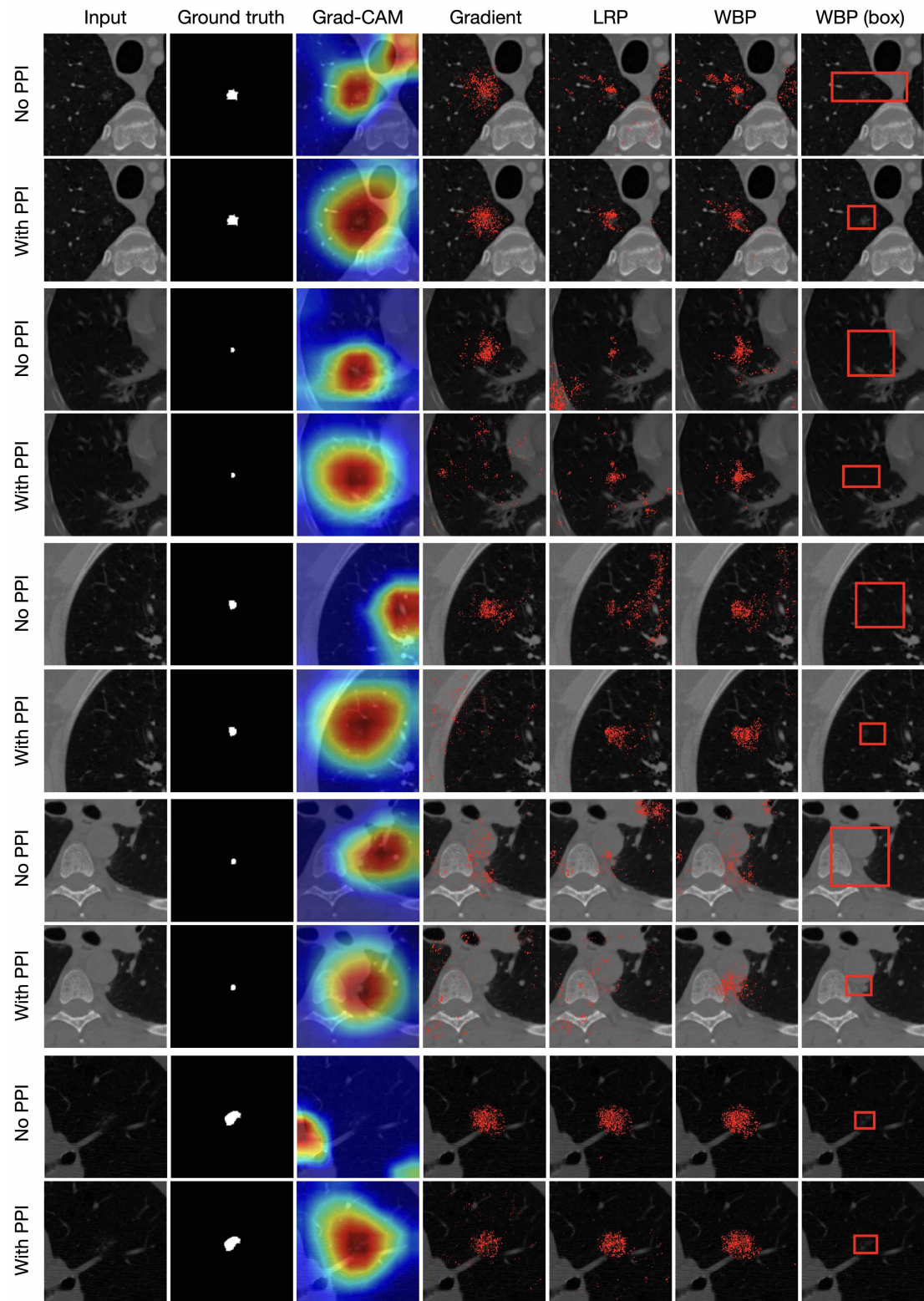


Figure 12: Comparison examples of saliency maps on LIDC dataset based on model trained with and without PPI. PPI saliency maps to focus on lesions.